

(2)

# Optical Processing of MMW for Agile Beamsteering and Beamforming

Contract No. N00014-93-C-0136

*Period of Performance:* 07/02/93 to 01/02/94

**AD-A277 161**

## Final Report



*Reporting Period:* 07/02/93 to 01/02/94

*Presented to:*

Office of Naval Research  
800 North Quincy Street  
Arlington, VA 22217-5660

**DTIC  
ELECTE  
MAR 21 1994  
S E D**

*Presented by:*

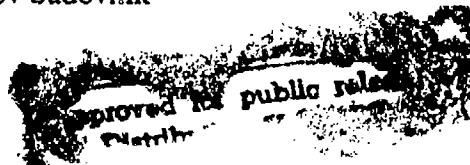
Physical Optics Corporation  
Research and Development Division  
20600 Gramercy Place, Suite 103  
Torrance, California 90501

**94-08791**



*Principal Investigator:*

Lev Sadovnik



**February 1994**

**DTIC QUALITY INSPECTED 1**

*Research supported by Strategic Defense Initiative/Innovative Science and Technology and  
managed by the Office of Naval Research.*

**94 3 18 106**

Enl Rpt 0294.3226 SDI-AGILE

## 1.0 INTRODUCTION

There is little doubt that an electronically steered, stationary scanning antenna offers significant advantages over any gimbaled installation, especially for tactical missile seekers. A scanning phased array antenna reduces the demands on space and power and makes better use of the space available.

It is widely believed that the millimeter wave (MMW) band (W-band) is the region of the RF spectrum which provides the best angular resolution. In fact, MMW sensor and seeker technologies have made significant advances in recent years, demonstrating their suitability for autonomous, adverse weather, battlefield, and smart munition applications. Moreover, only the use of the W-band can produce an active seeker with imaging capability for on-board target identification [1]. Figure 1-1 illustrates the use of a MMW seeker for terminal guidance.

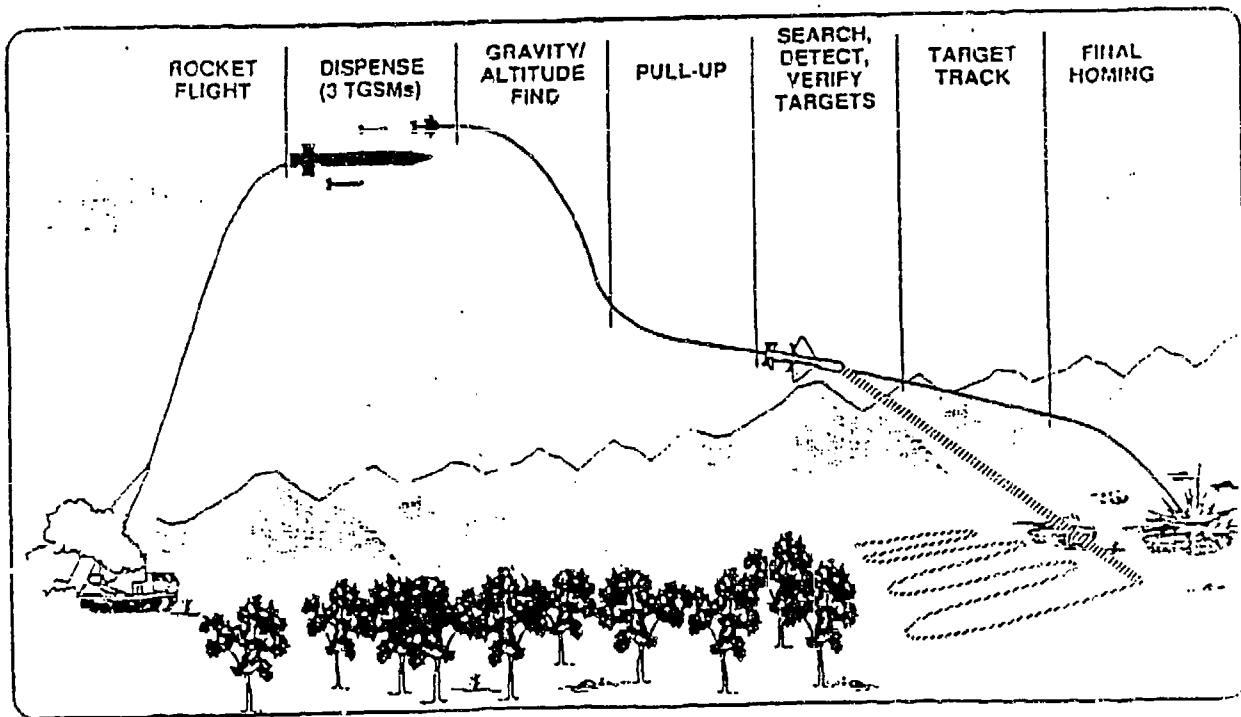


Figure 1-1  
Artist's conception of a multiple launch rocket system with  
a terminally guided submunition (TGS) [2].

Active homing can be fully autonomous, as shown in Figure 1-2. The missile contains the complete radar system, including a transmitter. The disadvantages of active homing are that an

expensive transmitter is lost with each round and that the maximum range is short, about 10 km, because of the small antenna and the limited transmitter power.

Another method of air-to-ground homing guidance is to separate the transmitter from the missile and to install the transmitter permanently at, or near, the launch point, as shown in Figure 1-3. The price paid for utilizing only one transmitter for multi-launch attack is the loss of autonomy.

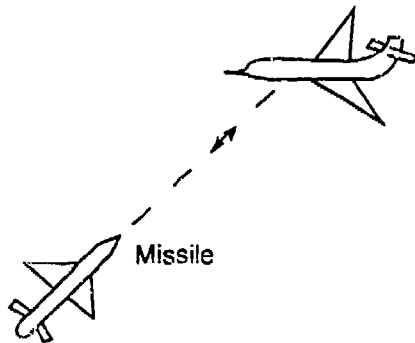


Figure 1-2  
 Active homing guidance.

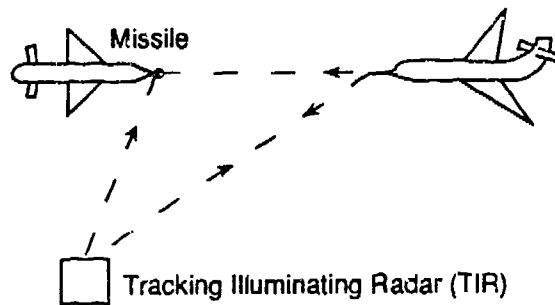


Figure 1-3  
 Semi-active homing guidance.

Clearly, an inexpensive transmitter would solve the above dilemma, especially in the millimeter wave (MMW) region where W-band radar, although expensive, offers higher resolution (compared to the K-band) and lower vulnerability to weather (compared to IR imaging).

A quantitative comparison of seeker operation in the microwave, MMW, and IR spectral regions is given in Table 1-1 [3].

Accession For	
NTIS	<input checked="" type="checkbox"/>
CRA&I	<input checked="" type="checkbox"/>
DTIC	<input type="checkbox"/>
TAB	<input type="checkbox"/>
Unannounced	<input type="checkbox"/>
Justification .....	
By .....	
Distribution /	
Availability Codes	
Dist	Avail and/or Special
A-1	

Table 1-1 Comparison of Seeker Operation in Three Spectral Regions

Radar/Radiometer Capability	Microwave	MMW	IR
Volume Search	Good	Fair	Poor
Classification/Identification	Poor	Fair	Good
Tracking Accuracy	Poor	Fair	Good
Adverse Weather Performance	Good	Fair	Poor
Smoke Performance	Good	Good	Poor
Covert Capability	Poor	Good	Good
Day/Night Performance	Good	Good	Fair

Clearly, the MMW spectral band represents a trade off. It provides a seeker with acceptable performance in all of the required functions. Table 1-2 shows that MMW/IR sensor fusion utilizing a single antenna would be an even more attractive approach.

The development of the MMW semiconductor antenna, begun by POC in this Phase I project, will have the potential to provide IR beamsteering as well. This expansion of the antenna's functions promises to be of immense value for future development. In fact, several artillery and rocket launched systems which combine MMW and IR sensors are currently under development [2] (see Table 1-2).

Table 1-2 IR/MMW Sensors for "Smart" Munitions (Compiled from Open Sources)

SYSTEM	COUNTRY	CALIBER (MM)	GUIDANCE	SENSOR	RANGE	TARGETS	STATUS
155 ACED	France	155	Sensor Fuzed	IR/MMW	25 km	Armor	Development
EAP	Germany	155	TGM	MMW		Armor	Feasibility
EPHRAM	Germany	155	TGM	IR/MMW			Ceased Dev.
HABICHT	Germany	203/155	Sensor Fuzed	IR/MMW		Armor	Ceased Dev.
LARS 110 TGW	Germany	102 MRL	TGM	IR	25 km	Armor	Development
SMARt 155	Germany	155	Sensor Fuzed	IR/MMW		Armor	Development
ZEPL	Germany	203/155	Sensor Fuzed	IR/MMW			Ceased Dev.
CLAMP	Israel	155	TGM	SAL	20 km	Armor	Development
ULYSSES	Italy/UK	122 MRL	TGM	MMW	34 km	Armor	Development
APGM	NATO	155	TGM	IR/MMW	24 km	Pt. Tgts	Ceased Dev.
BONUS	Sweden	155	Sensor Fuzed	IR	24 km	Armor	Unknown
BOSS	Sweden	155	TGM		>20 km	Armor	Development
MLRS TGW	US/UK/GE/FR	MRL	TGSM	MMW	30 km	Armor	Development

MRL - multiple rocket launcher  
TGM - terminal guided weapon  
TGSM - terminally guided submunition  
SAL - semiactive laser

## 2.0 POC'S CONCEPT

POC proposed to look at the problem from another perspective. Rather than imposing a millimeter-wave frequency on a light carrier, the direct optical modulation of millimeter waves was examined. Two theoretically and experimentally proven premises form the foundation of POC's patented [4] technology:

- The MMW transmittance/reflectance of a semiconductor material can be dramatically changed (by more than several orders of magnitude) by illuminating it with light whose photon energy is greater than the semiconductor's bandgap.
- Phase shifting is not the only way to control the direction and shape of a MMW beam. MMW beamforming and beamsteering can be achieved through MMW amplitude modulation only.

POC's novel millimeter wave diffraction concept can be explained with the use of several drawings, starting from a simple embodiment and gradually moving toward a more complete design. Setting aside the nature of the grating material (assume a metal grating for simplicity), we can state that a grating will diffract MMW beam according the equation

$$\sin \phi + \sin \theta = m\lambda / \Lambda \quad , \quad (2-1)$$

where  $m = 0; \pm 1; \dots$  is the diffraction order number ( $m = 0$  corresponds to the zero order, the undiffracted beam) (see Figure 2-1), and  $\Lambda$  is the grating period. The same diffraction pattern is produced by reflection from a grating (Figure 2-2).

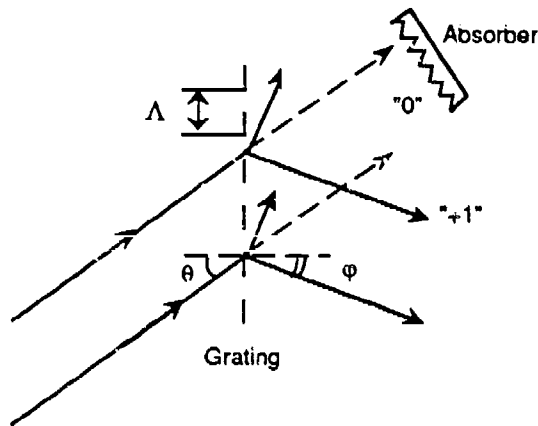


Figure 2-1  
MMW diffraction by a transmission grating.

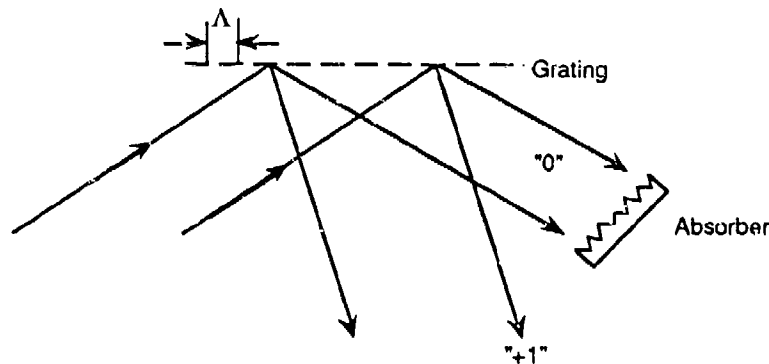


Figure 2-2  
MMW diffraction by a reflection grating.

Here, an absorber is introduced to eliminate mirror (Fresnel) reflection, to concentrate our attention on the diffracted beam. The main conclusion we would like to draw from these two figures is that the direction of an output diffracted beam (for a fixed wavelength and input incidence angle) is determined by the grating period. By varying the grating period, a MMW diffracted beam can be steered in accordance with Eq. (2-1).

In the next step, a very shallow incident beam can be thought of as being confined in a waveguide (Figure 2-3), so that a grating can couple it out. Once again, the direction of the output beam varies with the grating period  $\Lambda$ . Although in a single-mode waveguide MMWs do not really reflect from boundaries, their behavior is described by

$$\sin \phi = n_{\text{eff}} + \frac{\lambda}{\Lambda} , \quad (2-2)$$

where  $n_{\text{eff}}$  is the waveguide's effective refractive index. Again, by controlling the grating parameters, the amplitude and phase of the MMW antenna field can be controlled as well.

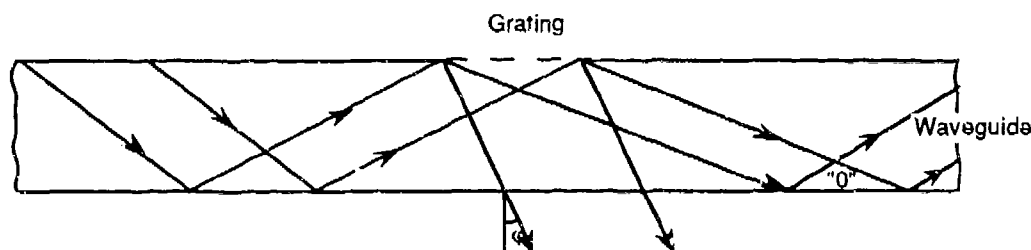


Figure 2-3  
Waveguide grating coupler geometry.

This principle, in a more elaborate form, provides the foundation for POC's proposed guided-wave antenna induced by light (GAIL). The principal idea is to couple MMW radiation out of a semiconductor waveguide into free space using a grating coupler induced by light. This is similar to a slot array which leaks radiation from a traveling wave antenna or an array of metal strips in a microstrip antenna design. The main difference here is that, in contrast to those antennas, GAIL has the flexibility to rapidly change its radiation pattern, and is thus capable of agile beamsteering and beamforming.

### 3.0 PHASE I RESULTS

The Phase I goal was to demonstrate the feasibility of POC's GAIL concept through computer simulation and laboratory experiments. In this section, we describe the main results of Phase I:

- The development of a rigorous theoretical model of the changes in the MMW dielectric permittivity of a semiconductor when it is illuminated by light.
- The calculation of optimized semiconductor parameters to maximize its MMW response to light illumination.
- The experimental demonstration of the control of MMW modulation by light.

#### 3.1 Theoretical Model

As a first step, we developed a theoretical model for the changes in MMW transmittance and reflectance of a semiconductor when it is illuminated with light. The geometry of the illumination of the silicon slab is shown in Figure 3-1.

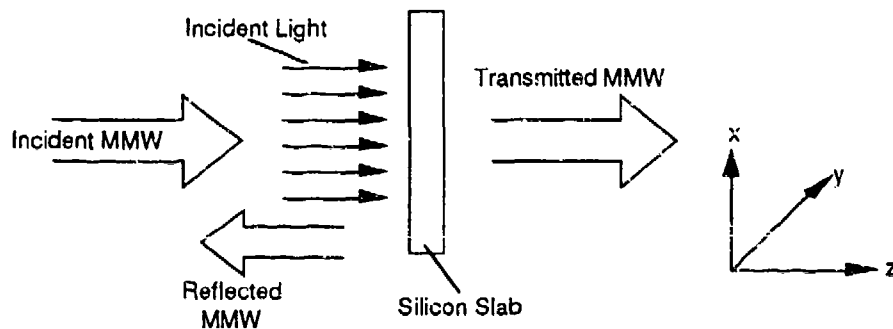


Figure 3-1  
Geometry of the simulation of changes in MMW transmittance and reflectance due to light pumping.

When the MMW impinges on the silicon slab (in the z direction), the equation governing the electric field distribution is

$$\frac{\partial^2 E}{\partial z^2} + \frac{\omega^2}{c^2} \epsilon(z) E = 0 \quad , \quad (3-1)$$



where  $E$  is the electric field,  $\omega$  is the frequency of the MMW,  $c$  is the velocity of light, and  $\epsilon(z)$  is the distribution of the dielectric function in the  $z$  direction.

In the classical approximation for an infinite medium the solution of Eq. (3-1) is

$$E = \frac{\text{Const}}{\sqrt[4]{f(z)}} \exp\left(i \int_0^z \sqrt{f(z)} dz\right), \quad (3-2)$$

while for a slab of thickness  $d$ , the solution takes the form

$$\begin{aligned} E = & \frac{\sqrt[4]{f(0)}}{\sqrt[4]{f(z)}} E_0 \exp\left(i \int_0^z \sqrt{f(z)} dz\right) \\ & + E_d \frac{\sqrt[4]{f(d)}}{\sqrt[4]{f(z)}} \exp\left(i \int_0^d \sqrt{f(z)} dz\right), \end{aligned} \quad (3-3)$$

where  $f(z) \equiv \frac{\omega^2}{c^2} \epsilon(z)$ , and  $E_0$  and  $E_d$  are the electric fields at the boundaries of the slab. The vector potential can be expressed as

$$\begin{aligned} A = & \frac{c}{i\omega} E \\ = & \frac{c \exp(-i\omega t)}{i\omega \sqrt[4]{f(z)}} \left[ \frac{\sqrt[4]{f(0)}}{\sqrt[4]{f(z)}} E_0 \exp\left(i \int_0^z \sqrt{f(z)} dz\right) + E_d \frac{\sqrt[4]{f(d)}}{\sqrt[4]{f(z)}} \exp\left(i \int_z^d \sqrt{f(z)} dz\right) \right], \end{aligned} \quad (3-4)$$

and, correspondingly, the magnetic field is

$$H = H_y = \frac{\partial A}{\partial z}. \quad (3-5)$$

From Eqs. (3-3), (3-4) and (3-5),

$$\begin{aligned} H_y = & \frac{c}{\omega} \exp(-i\omega t) \left\{ E_0 \frac{\sqrt[4]{f(0)f(z)}}{\sqrt[4]{f(z)}} \exp\left(i \int_0^z \sqrt{f} dz\right) - E_d \frac{\sqrt[4]{f(d)f(z)}}{\sqrt[4]{f(z)}} \exp\left(i \int_z^d \sqrt{f} dz\right) \right\} \\ E_x = & \exp(-i\omega t) \left\{ E_0 \frac{\sqrt[4]{f(0)}}{\sqrt[4]{f(z)}} \exp\left(i \int_0^z \sqrt{f} dz\right) + E_d \frac{\sqrt[4]{f(d)}}{\sqrt[4]{f(z)}} \exp\left(i \int_z^d \sqrt{f} dz\right) \right\} \end{aligned} \quad (3-6)$$

Let  $i$ ,  $r$ , and  $t$  be the amplitudes of the incident, reflected and transmitted waves, respectively. The boundary conditions at  $z = 0$  and at  $z = d$  yield the system of equations

$$\begin{aligned} E_i + E_r &= E_0 + E_d \sqrt{\frac{\epsilon(d)}{\epsilon(0)}} \exp\left(i \frac{\omega}{c} \int_0^d \sqrt{\epsilon} dz\right) \\ H_i + H_r &= E_0 \sqrt{\epsilon(0)} - E_d \sqrt{\epsilon(d)\epsilon(0)} \exp\left(i \frac{\omega}{c} \int_0^d \sqrt{\epsilon} dz\right) \\ E_t &= E_0 \sqrt{\frac{\epsilon(0)}{\epsilon(d)}} \exp\left(i \frac{\omega}{c} \int_0^d \sqrt{\epsilon} dz\right) + E_d \\ H_t &= E_0 \sqrt{\epsilon(0)\epsilon(d)} \exp\left(i \frac{\omega}{c} \int_0^d \sqrt{\epsilon} dz\right) - E_d \sqrt{\epsilon(d)} \\ H_i &= E_i \\ H_r &= -E_r \\ H_t &= E_t \end{aligned} \quad (3-7)$$

Finally, the transmittance of the silicon slab is

$$\begin{aligned} T &= \left| \frac{E_t}{E_i} \right|^2 \\ &= \frac{\left[ 16 \exp\left(-2 \frac{\omega}{c} g\right) \sqrt{(n_0^2 + \chi_0^2)(n_d^2 + \chi_d^2)} \right]}{\left[ (1 + n_0)^2 + \chi_0^2 \right] \left[ (1 + n_d)^2 + \chi_d^2 \right] \left\{ 1 + 4 \rho_0 \rho_d \exp\left(-4 \frac{\omega}{c} g\right) - 2 \exp\left(-2 \frac{\omega}{c} g\right) \sqrt{\rho_0 \rho_d} \cos\left(2 \frac{\omega}{c} f + \beta_0 + \beta_d\right) \right\}} \end{aligned} \quad (3-8)$$

where

$$\begin{aligned} n_{d,0} &\equiv n(d), n(0); \quad \rho_{d,0} \equiv \rho(d), \rho(0) \\ \chi_{0,d} &\equiv \chi(d), \chi(0); \quad \beta_{d,0} \equiv \beta(d), \beta(0) \\ n(z) &= \frac{1}{\sqrt{2}} \left[ \sqrt{(\epsilon')^2 + (\epsilon'')^2} + \epsilon' \right]^{\frac{1}{2}}, \\ \chi(z) &= \frac{1}{\sqrt{2}} \left[ \sqrt{(\epsilon')^2 + (\epsilon'')^2} - \epsilon' \right]^{\frac{1}{2}}, \\ \epsilon(z) &= \epsilon' + i\epsilon'', \\ \sqrt{\rho} &= \frac{\sqrt{(n^2 - 1 + \chi^2)^2 + 4\chi^2}}{(n+1)^2 + \chi^2}, \\ \beta &= \tan^{-1} \frac{2\chi}{n^2 - 1 + \chi^2}; \quad g = \int_0^d \chi(z) dz; \quad f = \int_0^d n(z) dz. \end{aligned}$$

In order to calculate the complex dielectric permittivity of the semiconductor, we use the Drude theory of electromagnetic field interaction with free electron gas [5]

$$\epsilon(z) = \epsilon_{\infty} \left[ 1 - \frac{\omega_n^2(z)}{\omega(\omega + i\tau_n^{-1})} - \frac{\omega_p^2(z)}{\omega(\omega + i\tau_p^{-1})} \right], \quad (3-9)$$

where  $\epsilon(z)$  is the complex dielectric permittivity,  $\epsilon_{\infty}$  is the dielectric permittivity of the silicon material in equilibrium. Also,

$$\tau_n = \mu_n \frac{m_n}{q} \quad \text{and} \quad \tau_p = \mu_p \frac{m_p}{q},$$

are electron and hole relaxation times,  $\mu_n$  and  $\mu_p$  are electron and hole mobilities,  $m_n$  and  $m_p$  are their effective masses,  $q$  is the electronic charge, and

$$\omega_n(z) \equiv \sqrt{\frac{q^2 \cdot N(z)}{m_n \epsilon_{\infty}}}$$

$$\omega_p(z) \equiv \sqrt{\frac{q^2 N(z)}{m_p \epsilon_{\infty}}},$$

where  $N(z)$  is the nonequilibrium carrier distribution that is generated due to the light flux  $\Phi$  incident on the silicon slab with a photon energy  $\hbar\omega$ :

$$N(z) = \frac{G\tau}{\alpha^2 L^2 - 1} \left[ A \exp\left(-\frac{z}{L}\right) + B \exp\left(\frac{z}{L}\right) - \exp(-\alpha z) \right] + N_0. \quad (3-10)$$

Here  $G = (1 - R) \frac{\Phi\tau}{\hbar\omega}$  is the generation rate,  $L$  is the volume diffusion length, and  $\tau$  is the carrier lifetime. The coefficients in Eq. (3-10) are

$$A = \frac{[(S + \alpha D)(D/L + S)\exp(d/L) + (S + \alpha D)(D/L + S)\exp(-\alpha d)]}{2(S^2 + D/\tau)\sinh(d/L) + (2sD/\tau)\cosh(d/L)} \quad \text{and}$$

$$B = \frac{[(S + \alpha D)(D/L + S)\exp(-d/L) + (S + \alpha D)(D/L + S)\exp(-\alpha d)]}{2(S^2 + D/\tau)\sinh(d/L) + (2sD/\tau)\cosh(d/L)}.$$

The ambipolar diffusion coefficient  $D$  can be expressed through the diffusion coefficients for electrons and holes  $D_n$  and  $D_p$  as  $D = (2D_n + D_p)/(D_n + D_p)$ . In Eq. (3-10),  $\alpha$  is the light absorption coefficient [6],  $N_e$  is the equilibrium carrier density, and  $S$  is the surface recombination rate.

Eqs. (3-8) and (3-10) were analyzed to determine how MMW transmittance and reflectance are affected by silicon material parameters such as carrier lifetime and surface recombination rate. The MMW frequency was assumed to be  $f = 94$  GHz.

The carrier lifetime  $\tau$  is a very important semiconductor parameter. In silicon,  $\tau$  can change over a wide range, from  $10^{-10}$  s (for a gold-compensated material) to more than  $10^{-3}$  s (for pure silicon grown with the floating zone technique). The magnitude of  $\tau$  determines the light power required to achieve the necessary changes in silicon's MMW transmittance.

The dependence of  $T$  on  $\tau$  is shown in Figure 3-2. At low illumination levels (curve a), transmittance is high, even for  $\tau = 10^{-3}$  s. At high illumination levels (curve c), total suppression of MMW transmittance can be realized even in silicon with  $\tau = 10^{-4}$  s, a typical value for silicon wafers used in microelectronics and solar cells.

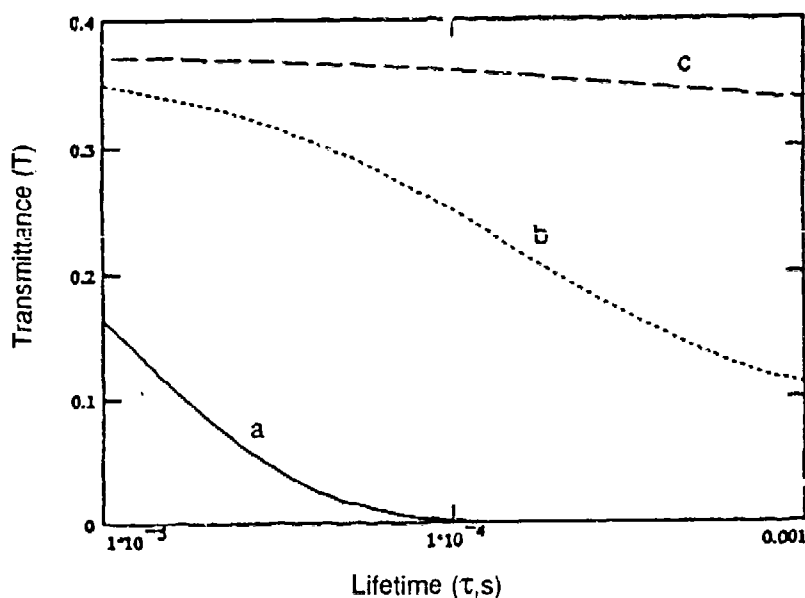


Figure 3-2  
 Dependence of MMW transmittance  $T$  on silicon carrier lifetime  $\tau$  at illumination levels of  
 (a)  $1 \text{ W/cm}^2$ , (b)  $10^{-1} \text{ W/cm}^2$ , and (c)  $10^{-2} \text{ W/cm}^2$ .

Using pure floating zone silicon with a lifetime of  $10^{-3}$  s totally suppresses MMW transmission, even at illumination levels between  $0.3$  and  $0.4$   $\text{W}/\text{cm}^2$ , as seen in Figure 3-3.

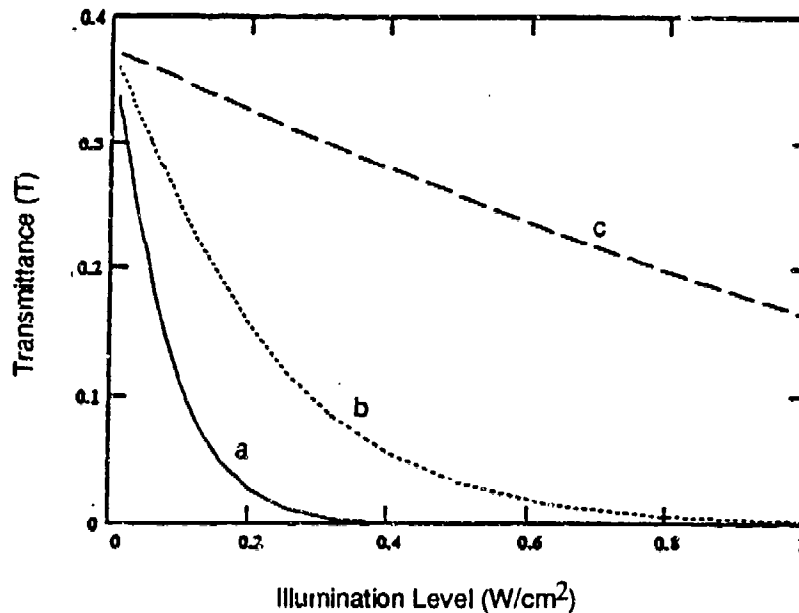


Figure 3-3  
Dependence of transmittance  $T$  on illumination level for silicon with carrier a lifetime of:  
(a)  $\tau = 10^{-3}$  s, (b)  $10^{-4}$  s, and (c)  $10^{-5}$  s.

The main conclusion to be drawn from Figure 3-3 is that good quality, non-compensated Si has to be chosen for the MMW antenna application. This will minimize the required illumination power. At the same time, the light pulse width must be adjusted to the material's carrier lifetime.

Yet another parameter which is important for the MMW antenna design is the wafer thickness  $d$ . The wafer thickness relates to the nonequilibrium electron-hole recombination rate. The relative contribution of volume recombination as compared to surface recombination depends on the wafer thickness. The MMW transmittance of the silicon wafer as a function of its thickness  $d$  and surface quality (surface recombination rate  $S$ ) can be seen in Figure 3-4. Quasi-periodical dependence on thickness can be explained by MMW interference within the slab. It can be seen that surface recombination plays an important role and can decrease the absorption, especially in the case of thin wafers. Thick wafers are less sensitive to surface recombination, which ranges from  $10^2$  to

$10^4$  cm/s. An  $S$  of  $10^2$  cm/s can be obtained with the use of special passivation techniques, such as surface barriers or the growth of a thick, very pure oxide layer. An  $S$  of  $10^4$  cm/s typically results from standard wafer processing.

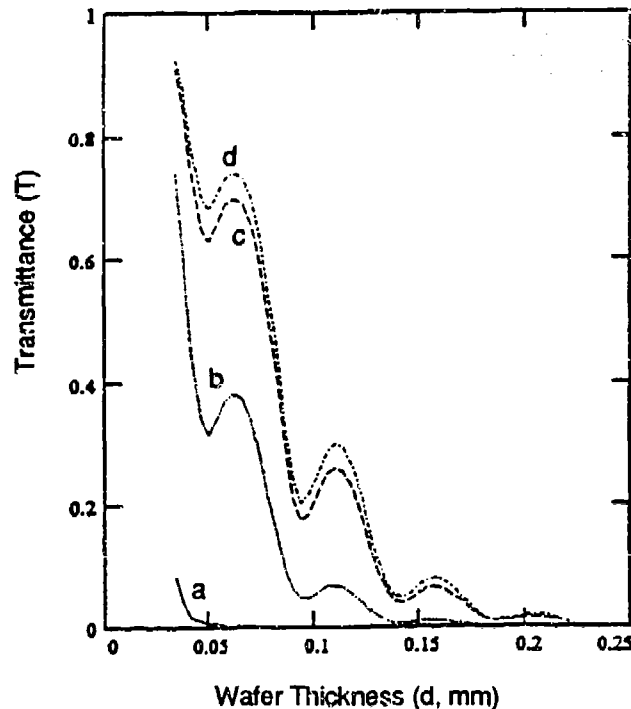


Figure 3-4  
Dependence of MMW transmittance  $T$  on silicon wafer thickness  $d$  for various surface recombination rates: (a)  $S = 10^2$  cm/s, (b)  $S = 10^3$  cm/s, (c)  $S = 10^4$  cm/s and (d)  $S = 10^5$  cm/s.

The relationship between the wafer thickness and attainable MMW transmittance suggests that wafers with a low surface recombination rate should be used.

Eq. (3-8) allows to compute the power requirements for the light illumination, and the influence of the illuminating light's wavelength on wafer transmittance. The results of the computation are plotted in Figure 3-5. The calculations were made for a thin silicon wafer ( $d = 0.064$  mm). In this case, light with smaller absorption coefficients ( $\alpha = 10$  to  $10^2$  cm $^{-1}$ , which corresponds to  $\lambda = 1.08$  and  $1.01$  mm, respectively) can suppress MMW transmission much more effectively than light of shorter wavelengths, which is absorbed farther from the surface, and generates carriers whose recombination is less dependent on surface recombination.

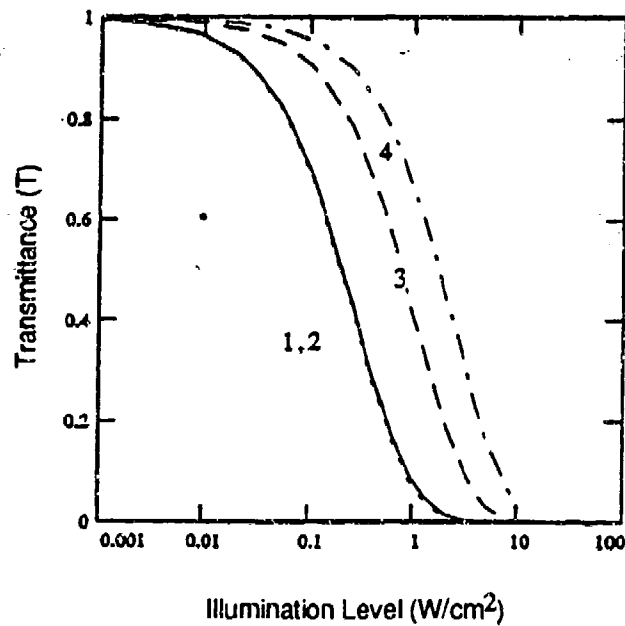


Figure 3-5  
Dependence of MMW transmittance on illumination level. Curves 1 to 4 correspond to various pumping light wavelengths: (1) 1.08 mm, (2) 1.01 mm, (3) 0.8 mm, and (4) 0.5 mm.

Using the calculated data, the silicon material we chose for the antenna fabrication must have the optimized parameters shown in Table 3-1.

Table 3-1 Parameters of Silicon Slab

Type of Conductivity	N-type (electronic)
Carrier Density	$P_0 = 10^{12} \text{ cm}^{-3}$
Carrier Lifetime	$\tau = 10^{-3}$
Dielectric Constant	$\epsilon = 11.8$
Diffusion Coefficient for Electrons	$D_n = 37.6 \text{ cm}^2 \text{ s}^{-1}$
Diffusion Coefficient for Holes	$D_p = 13.0 \text{ cm}^2 \text{ s}^{-1}$
Electron Mobility	$1300 \text{ cm}^2 \text{ V}^{-1} \text{ s}^{-1}$
Hole Mobility	$600 \text{ cm}^2 \text{ V}^{-1} \text{ s}^{-1}$
Electron Effective Mass	$0.26 m_0$
Hole Effective Mass	$0.39 m_0$
Surface Recombination Rate	$S = 10^2 \text{ to } 10^3 \text{ cm s}^{-1}$
Slab Thickness	$d = 2 \text{ mm}$

The above model served as the initial step in developing a theory of optically induced gratings within the silicon slab. The geometry of the silicon slab illumination is shown in Figure 3-6.

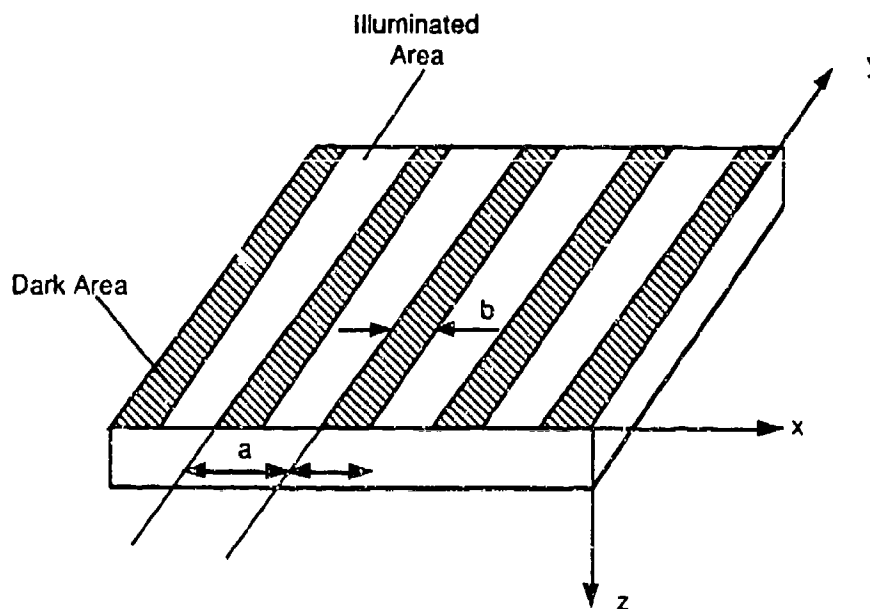


Figure 3-6  
Geometry of silicon slab illumination.



To determine the carrier distribution under illumination, we use an equation to characterize the distribution of nonequilibrium electron-hole pairs  $\Delta P(\vec{r})$ :

$$-D\nabla^2 \Delta P(\vec{r}) + \frac{\Delta P(\vec{r})}{\tau} = g(\vec{r}) \quad , \quad (3-11)$$

where  $g(\vec{r})$  is the rate of carrier generation per  $\text{cm}^3$ .

$$g(\vec{r}) = g(x, z) = g(x) \cdot \exp(-\alpha z), \quad (3-12)$$

where  $\alpha$  is the absorption coefficient for the pumping light. The particular solution of the inhomogeneous equation, Eq. (3-11), is

$$\Delta P(\vec{r}) = \frac{1}{(2\pi)^3} \int d^3k e^{i\vec{k}\vec{r}} \frac{g(\vec{k})}{Dk^2 + \frac{1}{\tau}} \quad . \quad (3-13)$$

For a periodic light pattern, as shown in Figure 3-6, generated by light with a photon flux density  $J_0$ ,

$$g(\vec{k}) = J_0 \cdot \alpha \cdot \delta(k_y) \frac{(2\pi)^2}{\alpha + ik_z} \left\{ \frac{\delta(k_x)(a-b)}{a} + \frac{1}{\pi} \sum_{k'=1}^{\infty} \frac{\sin[\pi k'(a-b)/a]}{k'} [\delta(k_x - k') + \delta(k_x + k')] \right\} \quad (3-14)$$

Substituting Eq. (3-14) into Eq. (3-13) gives

$$\begin{aligned} \Delta P(\vec{r}) = & \frac{J_0 \alpha (a-b) \tau}{2a(1 - \alpha^2 L^2)} \left\{ 2 \exp(-\alpha z) - (1 + \alpha L) \exp\left(-\frac{z}{L}\right) \right\} \\ & + \frac{J_0 \alpha}{\pi D} \sum_{k=1}^{\infty} \frac{\cos \frac{2\pi x k}{a} \sin \left[ \frac{\pi k(a-b)}{a} \right] \cdot L_k^2}{k(1 - \alpha^2 L_k^2)} \left\{ 2 \exp(-\alpha z) - (1 + \alpha L_k) \exp\left(-\frac{z}{L_k}\right) \right\} \quad , \end{aligned} \quad (3-15)$$

where  $L = \sqrt{D\tau}$  is the diffusion length and  $L_k^{-2} = L^{-2} + \frac{4\pi^2 k^2}{a^2}$ .

The general solution is:

$$\Delta P(\vec{r}) = \Delta P_n(\vec{r}) + C_1 \exp(-z/L) + C_2 \exp(z/L) \quad . \quad (3-16)$$

We use the boundary conditions

$$D \frac{d(\Delta P)}{dz} \Big|_{z=0} = s \Delta P|_{z=0} ,$$

and  $\Delta P_n \rightarrow 0$  for  $z \rightarrow \infty$ . Here,  $s$  is the surface recombination at the front surface, and surface recombination at the back surface, where  $\Delta P \rightarrow 0$ , is neglected. The final solution for  $\Delta P(x,z)$  is given by Eq. (3-17), which we used in our computer simulation.

$$\Delta P(x,z) = \frac{J_0 \alpha (a-b) \tau}{a(\alpha^2 L^2 - 1)} \left\{ \frac{\alpha L^2 + s\tau}{L + s\tau} \exp\left(-\frac{z}{L}\right) - \exp(-\alpha z) \right\} + \frac{J_0 \alpha}{\pi D} \sum_{k=1}^{\infty} \frac{\cos\left(\frac{2\pi x k}{a}\right) \sin\left(\frac{\pi k(a-b)}{a}\right) L_k^2}{k(\alpha^2 L^2 - 1)} \cdot (3-17)$$

$$\times \left\{ -2 \exp(-\alpha z) + \frac{(1 - \alpha L_k)(s L_k \tau - L^2)}{(L + s\tau) L_k} \exp\left(-\frac{z}{L}\right) + (1 + \alpha L_k) \exp\left(-\frac{z}{L_k}\right) \right\}.$$

In practice, we restricted the number of terms in the sum  $\sum_{k=1}^{\infty}$ . We found that, for the data listed in

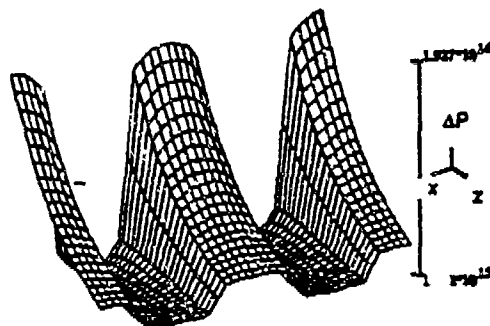
Table 3-2,  $k_{\max} = 250$  is a reasonable number, allowing a smooth solution for  $\Delta P$  and for the distribution of the optical constants to be calculated. (For a different set of data, it may be necessary to use  $k > 250$ .) Other parameters were as shown in Table 3-1.

Table 3-2 Light Induced Grating Parameters

Light Absorption Coefficient	$\alpha = 10^2$ to $10^3 \text{ cm}^{-1}$
Photon Flux	$J_0 = (1 \text{ to } 5) \times 10^{18} \text{ cm}^{-2}\text{s}^{-1}$
Illumination Strip Width	$a - b = 0.2$ to $0.4 \text{ cm}$
Illumination Grating Period	$a = 0.7 \text{ cm}$
MMW Frequency	$f = 94 \text{ GHz}$

Figures 3-7 through 3-11 represent the results of the computer simulation of the carrier distribution within the silicon slab under grating pattern illumination. The basic case is shown in Figure 3-7. Figures 3-8 to 3-11 differ from Figure 3-7 by one parameter only and demonstrate the impact of that parameter on the carrier distribution. Since the distribution is periodical, we show two grating periods only. Each of the five figures, Figures 3-7 through 3-11, contains one 3-D plot of the  $\Delta P(x,z)$  distribution and five cross-sections, three of which give the  $\Delta P$  distribution at the front surface, in the middle of the slab, and at the back surface, and two give the  $\Delta P$  distribution as the

function of the depth within the illuminated strips — one at the center of the illuminated area, the other at the center of the dark area.



$\Delta P(x,z), \text{ cm}^{-3}$

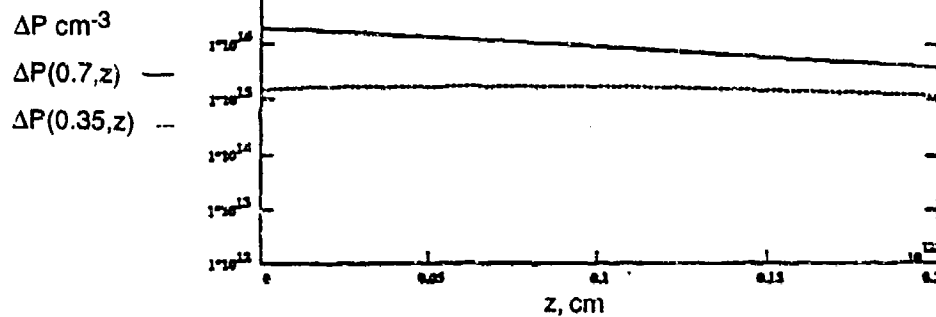
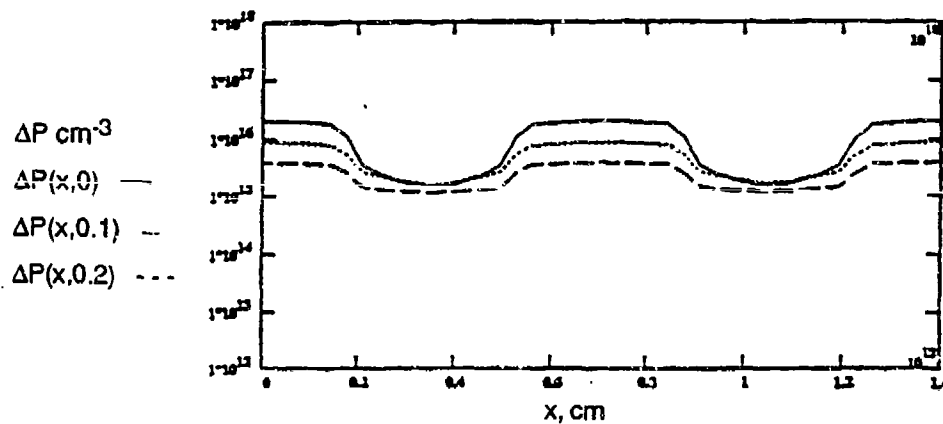


Figure 3-7

Carrier distribution within the silicon slab under grating pattern illumination. Basic case:  
 $P_0 = 1 \times 10^{12} \text{ cm}^{-3}$ ,  $J_0 = 5 \times 10^{18} \text{ cm}^{-2} \text{ s}^{-1}$ ,  $\alpha = 1 \times 10^3 \text{ cm}^{-1}$ ,  $\tau = 0.001 \text{ s}$ ,  $s = 100 \text{ cm s}^{-1}$ ,  
 $D = 19.32 \text{ cm}^2 \text{ s}^{-1}$ ,  $a = 0.7 \text{ cm}$ ,  $b = 0.35 \text{ cm}$ , and  $d = 0.2 \text{ cm}$ .

The basic case results in a high density of carriers across the whole slab, with a contrast between the illuminated and nonilluminated areas as high as  $dP = 1.8 \times 10^{16} \text{ cm}^{-3}$  and a small difference between the front surface and the other areas of the slab.

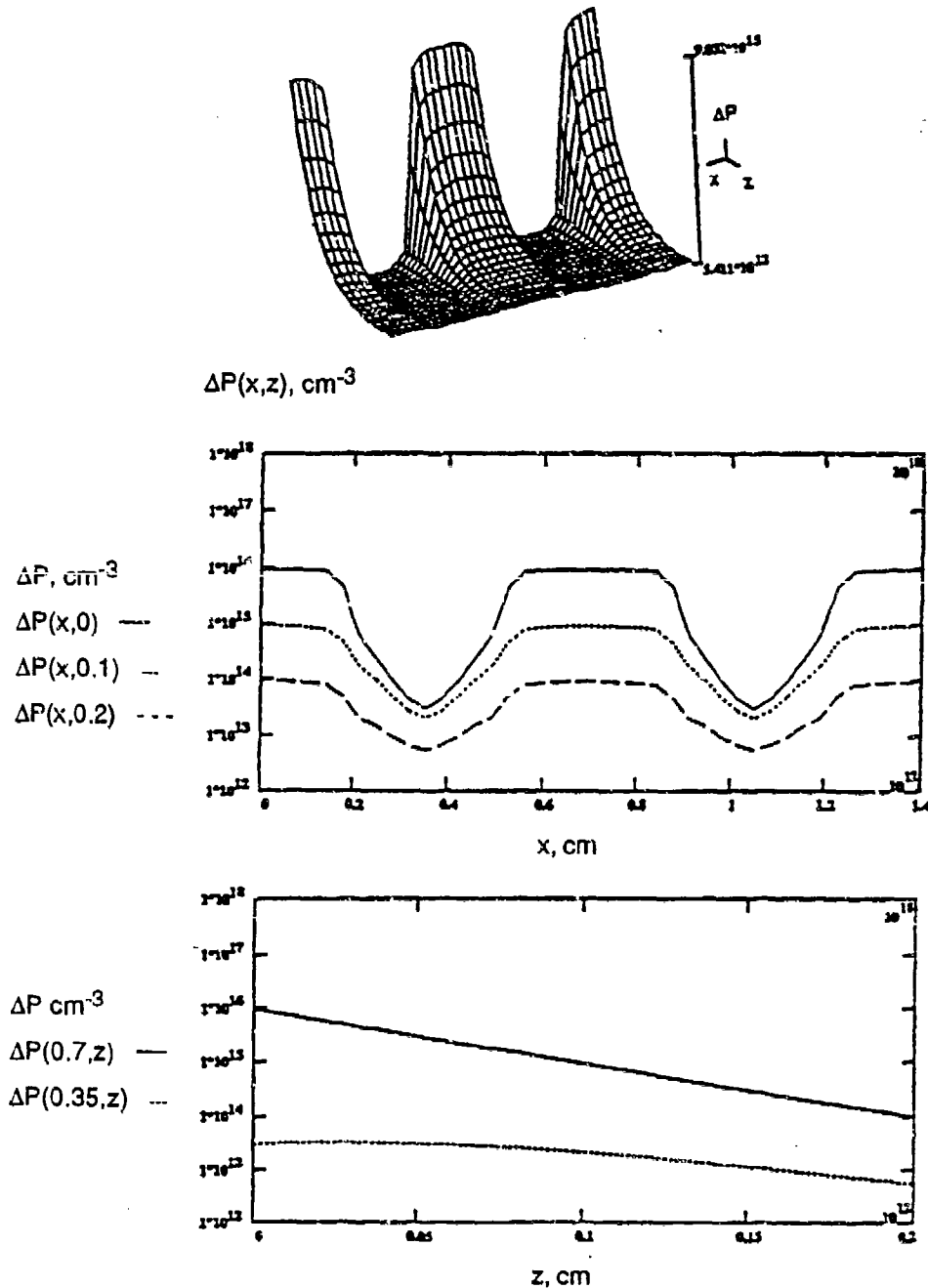


Figure 3-8  
Same as Figure 3-7, but the carrier lifetime is as low as  $\tau = 10^{-4} \text{ s}$ .

Lowering the carrier lifetime (Figure 3-8) results in a drop of carrier density across the whole slab, especially far from the front surface areas and in the unilluminated areas. The contrast  $\Delta P \approx 10^{16} \text{ cm}^{-3}$  is lower than in the basic case.

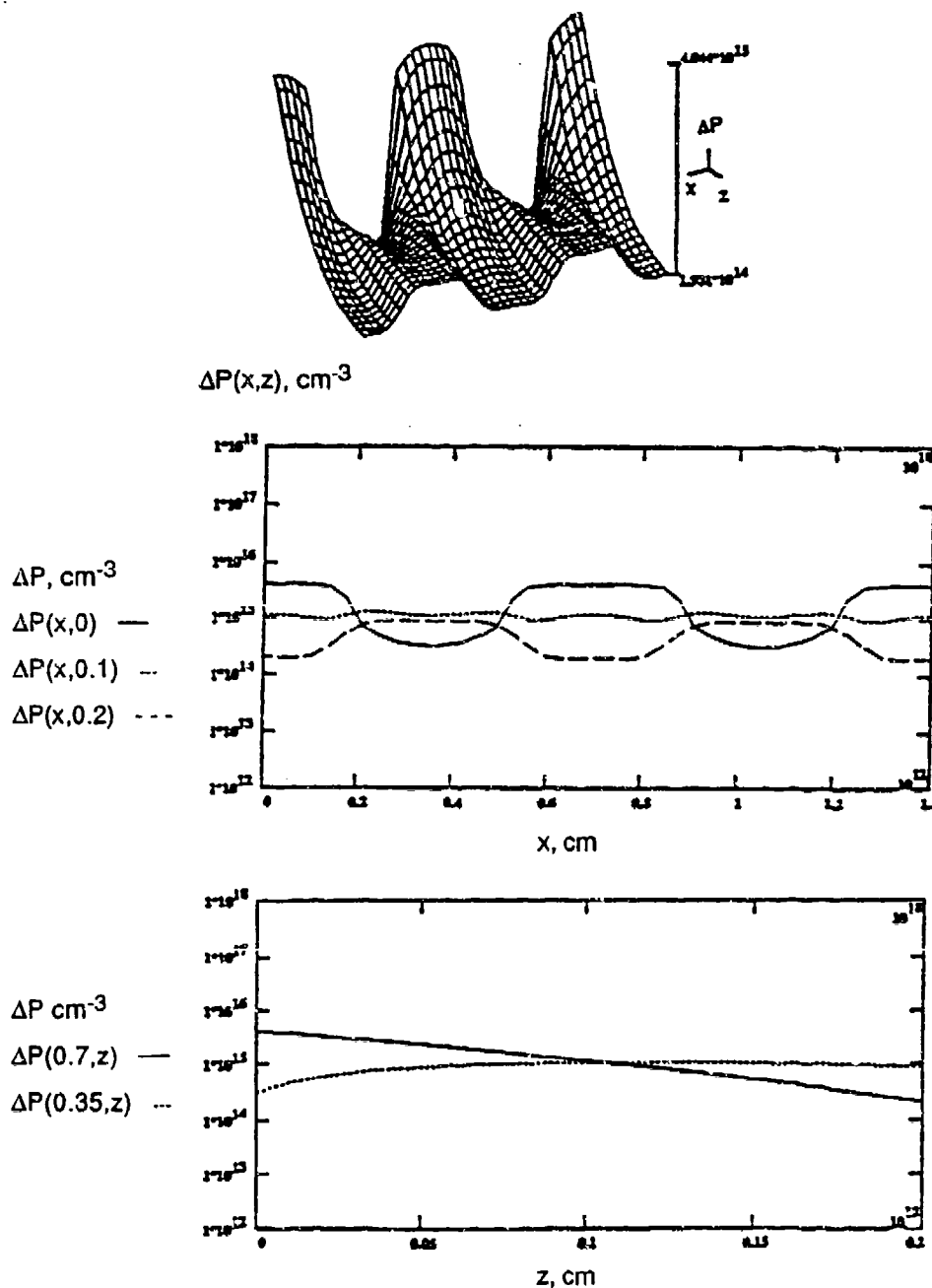


Figure 3-9  
Same as Figure 2-7, but the surface recombination rate  $s$  is as high as  $10^3 \text{ cm/s}$ .

A rise in surface the recombination rate (Figure 3-9) results in a drastic drop in carrier density and contrast which is lower than  $\Delta P = 0.4 \times 10^{16} \text{ cm}^{-3}$ .

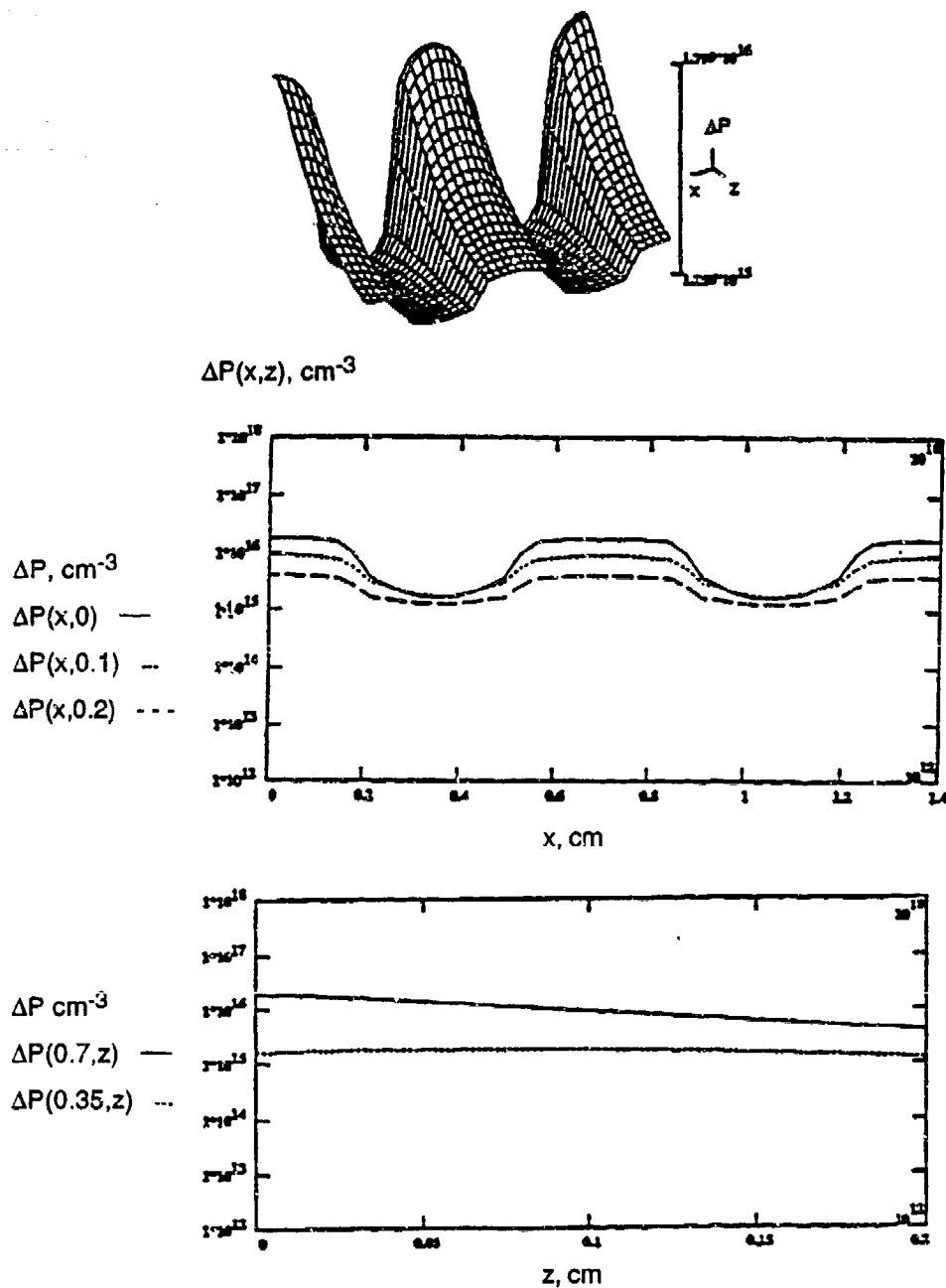


Figure 3-10  
Same as Figure 2-7, but with low absorption of the illuminating light.

A change in the absorption coefficient of the illuminating light from  $10^3 \text{ cm}^{-1}$  to  $10^2 \text{ cm}^{-1}$  (Figure 3-10) results in a small change in carrier distribution.

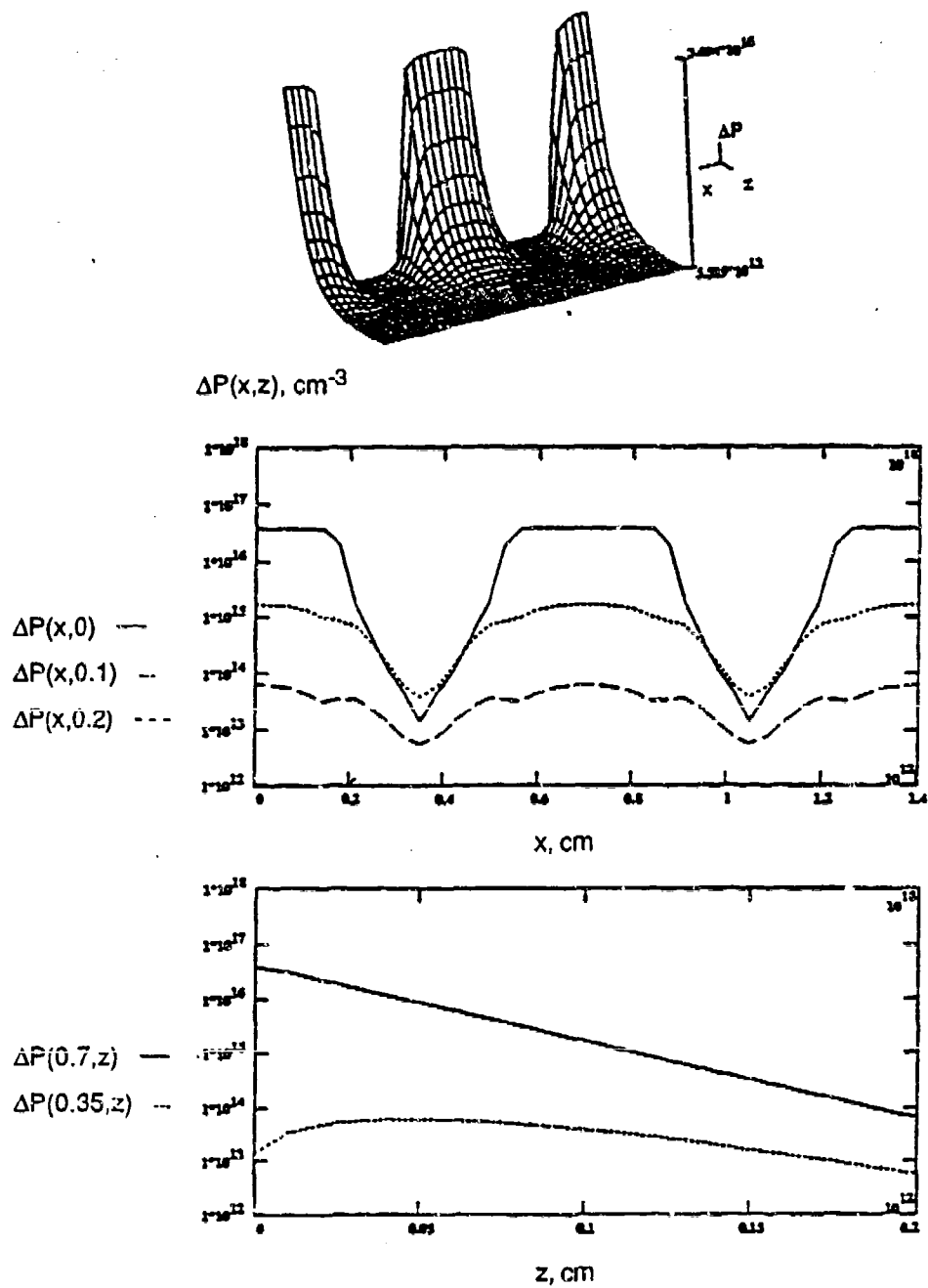


Figure 3-11

Same as Figure 3-7, but the diffusion coefficient  $D$  is reduced by a factor of 20 to  $D = 1 \text{ cm}^2\text{s}^{-1}$ .

Lowering the diffusion coefficient results in a high contrast between illuminated and nonilluminated areas because the light-induced grating is prevented from spreading. This is clearly

seen by comparing Figure 3-11 and Figure 3-7. Similar results can be obtained for dynamic situations where the pumping light pulse is shorter than the carrier lifetime. In this case, immediately after the pumping pulse, the carrier distribution will be similar to that shown in Figure 3-11, with high contrast between illuminated and nonilluminated areas.

In the next step, we again used the Drude model of light-carrier interaction to calculate the 2-D distribution of the complex dielectric permittivity  $\epsilon(x,z)$ . As in Eq. (3-9),

$$\epsilon(x,z) = \epsilon_0 \left[ 1 - \frac{\omega_n^2(x,z)}{\omega(\omega + i \cdot \tau_n^{-1})} - \frac{\omega_p^2(x,z)}{\omega(\omega + i \cdot \tau_p^{-1})} \right] . \quad (3-18)$$

The most interesting optical coefficients for our application are the refractive index  $n$  and the absorption coefficient  $\alpha_{MMW}$ . These are derived from the dielectric permittivity. The refractive index  $n$  can be obtained from the formula

$$n(x,z) = \text{Re} \sqrt{\epsilon(x,z)} . \quad (3-19)$$

The absorption coefficient for MMW is

$$\alpha_{MMW}(x,z) = \frac{4\pi}{\lambda} \text{Im} \sqrt{\epsilon(x,z)} , \quad (3-20)$$

where  $\lambda$  is the MMW wavelength.

Using Eqs. (3-17), (3-18) and (3-19), we calculated the  $n(x,z)$  and  $\alpha_{MMW}(x,z)$  distributions. The distributions for the basic case (corresponding to the  $\Delta P$  distribution in Figure 3-7) are shown in Figure 3-12.



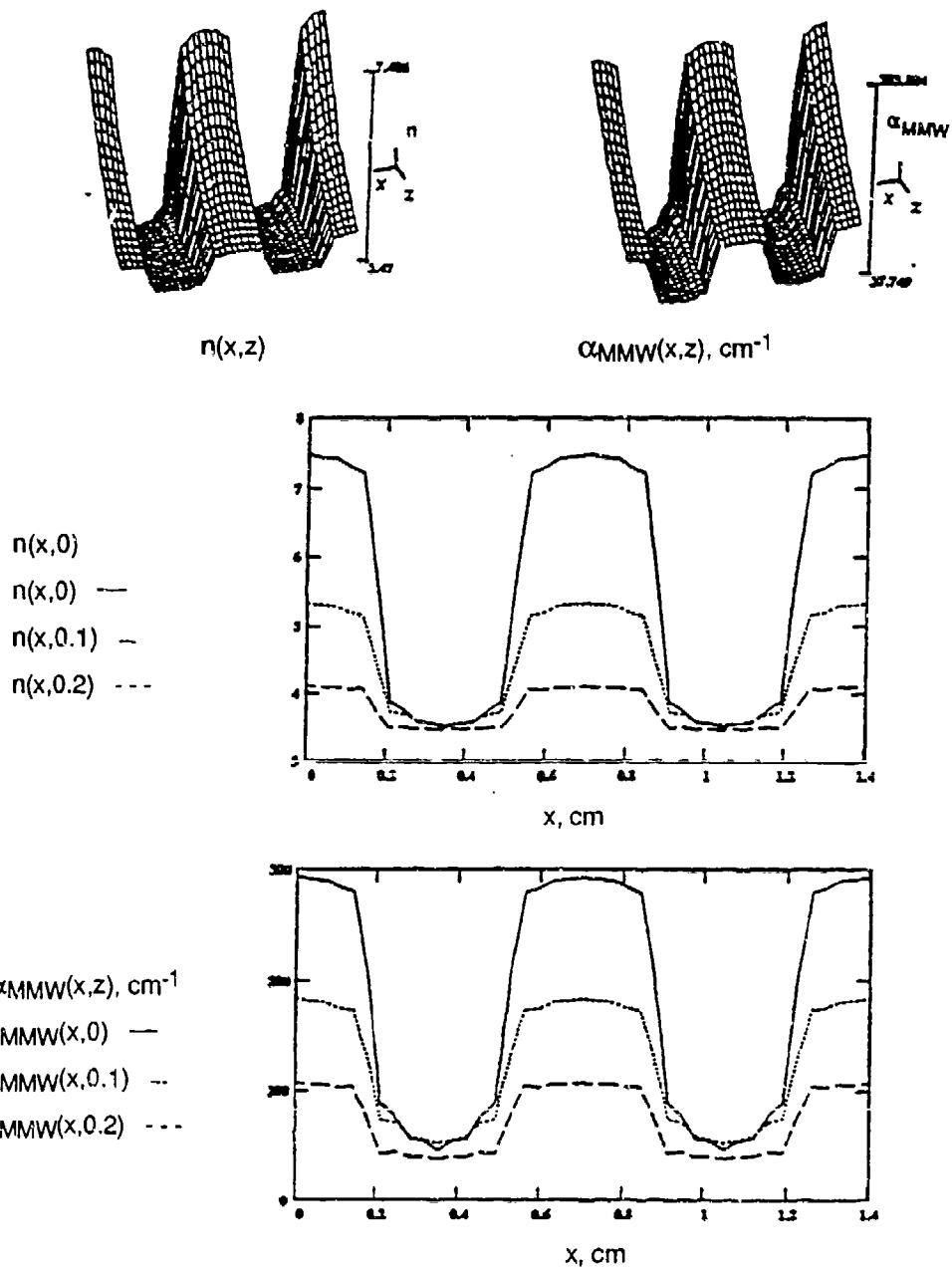


Figure 3-12

Distribution of the refractive index  $n(x,z)$  and absorption coefficient  $\alpha_{MMW}(x,z)$  for MMW grating pattern illumination. The values used for the calculation are  $f = 9.4 \times 10^{10}$ ,  $P_0 = 1 \times 10^{12} \text{ cm}^{-3}$ ,  $J_0 = 5 \times 10^{18} \text{ cm}^{-2} \text{ s}^{-1}$ ,  $\alpha = 1 \times 10^3 \text{ cm}^{-1}$ ,  $\tau = 0.001 \text{ s}$ ,  $s = 100 \text{ cm s}^{-1}$ ,  $D = 19.32 \text{ cm}^2 \text{ s}^{-1}$ ,  $a = 0.7 \text{ cm}$ ,  $b = 0.35 \text{ cm}$ , and  $d = 0.2 \text{ cm}$ .

The grating contrast depends on the material parameters in the same way that  $\Delta P(x,z)$  does. This can be seen from Figures 3-13 to 3-16.

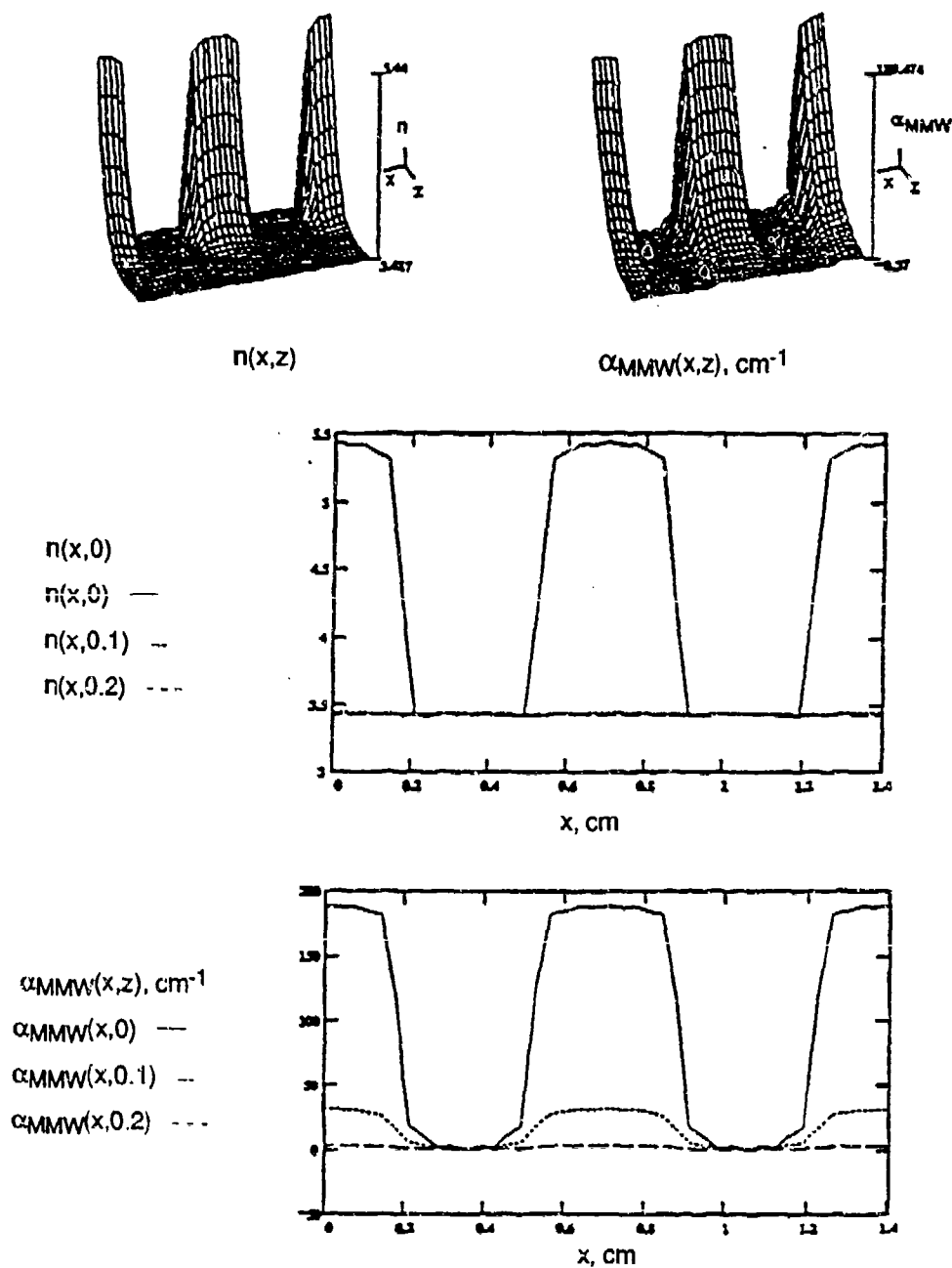


Figure 3-13  
Same as Figure 3-12, but the carrier lifetime  $\tau$  is  $10^{-4}$  s.

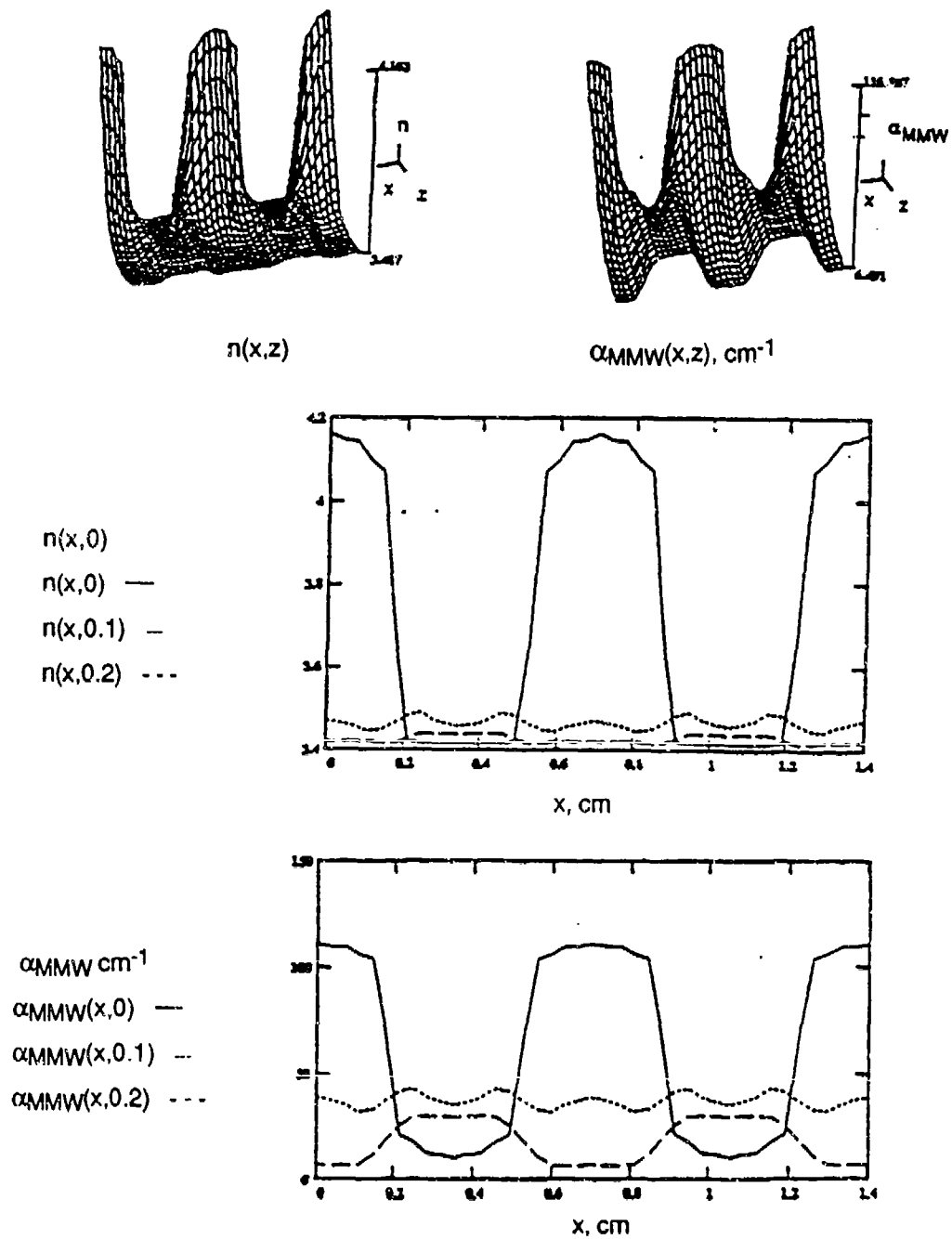


Figure 3-14  
Same as Figure 3-12, but the surface recombination is  $s = 10^3 \text{ cm s}^{-1}$ .

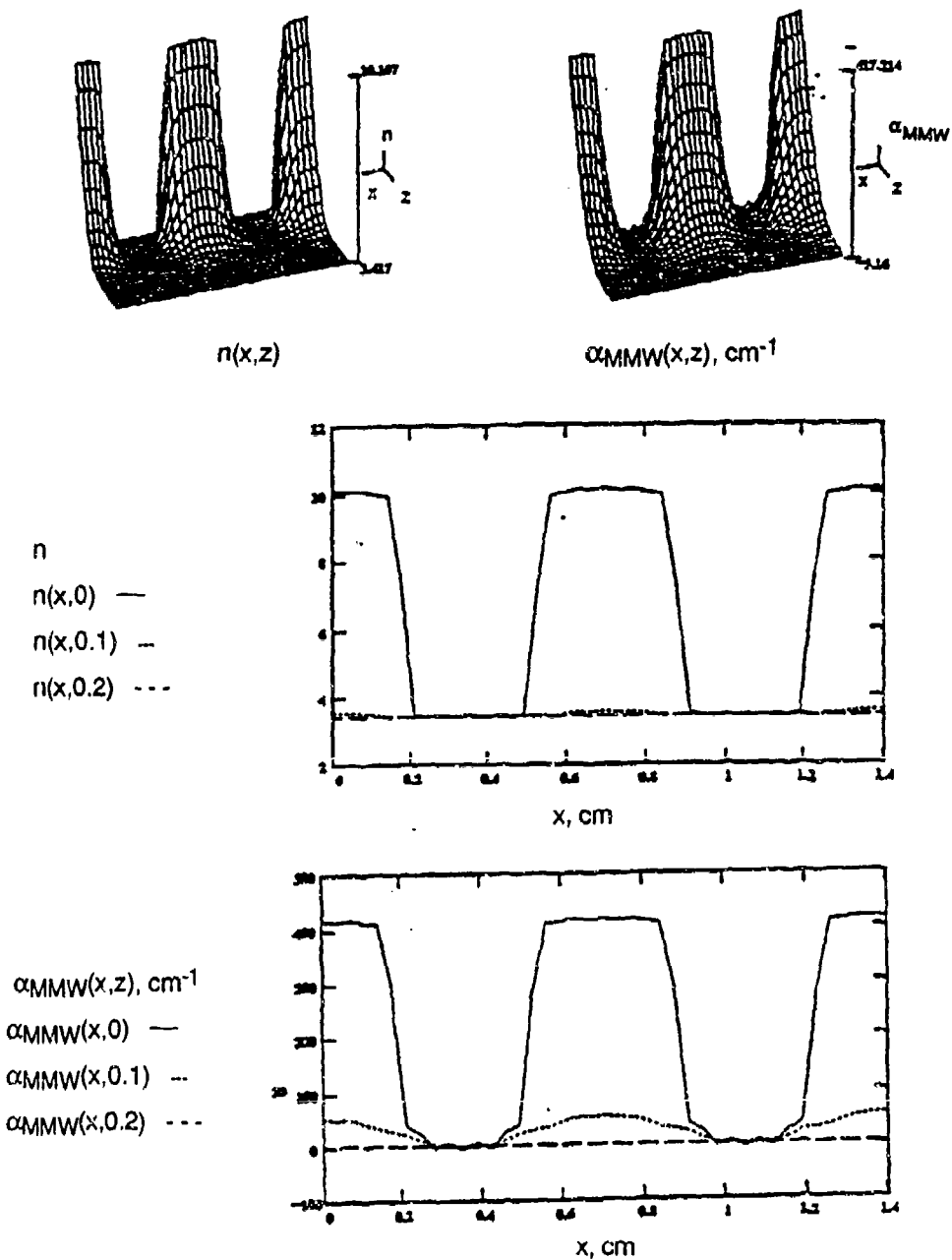


Figure 3-15  
Same as Figure 3-12, but the diffusion coefficient is  $D = 1 \text{ cm}^2\text{s}^{-1}$ .

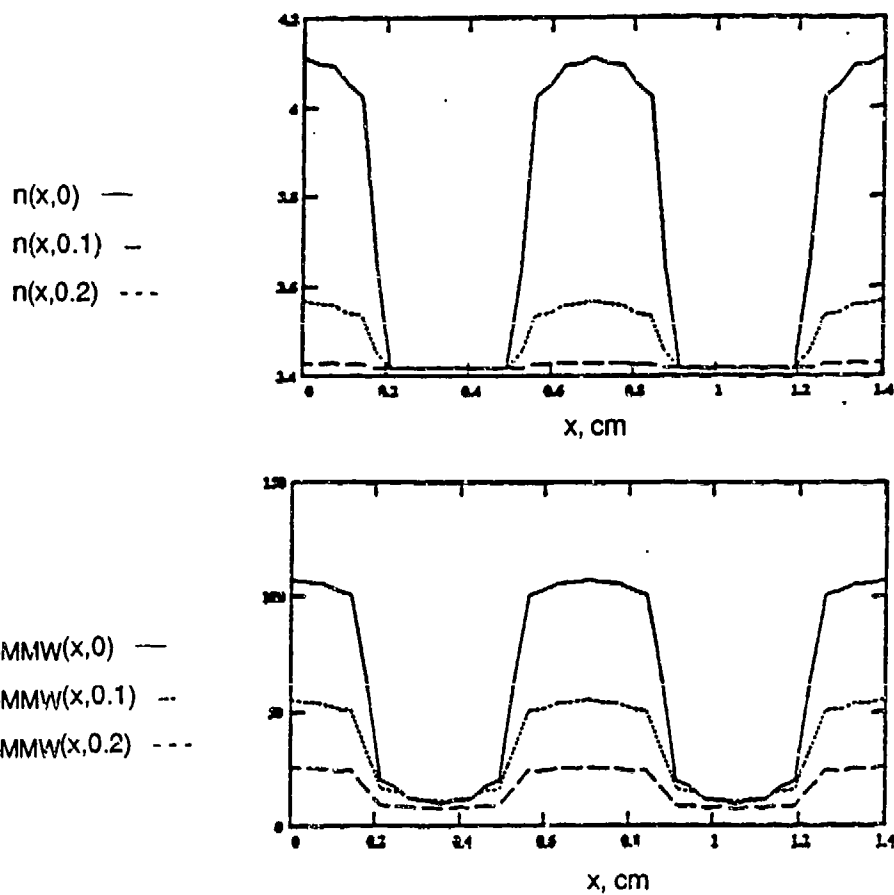
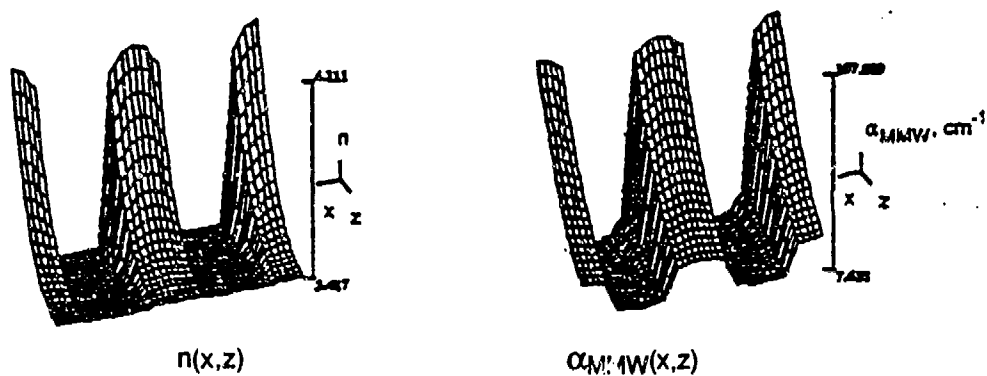


Figure 3-16.  
 Same as Figure 3-12 but the illumination flux is  $J_0 = 1 \times 10^{18} \text{ cm}^{-2}\text{s}^{-1}$ .

In conclusion, the performed simulation shows that the desired grating pattern can be photogenerated inside a silicon slab. Specifically, the results of the computer simulation showed that

- 1) The transmittance of MMW through a silicon wafer can be effectively modulated by the illumination absorbed within the silicon material. In the next section we will describe the experimental proof of this statement.
- 2) The pattern of the pumping illumination can be imposed on a wafer to obtain a grating for millimeter wave diffraction.

### 3.2 Experimental Demonstration of MMW Modulation by Light

The results obtained by the computer simulation were confirmed by the series of experiments described below. The experimental setup is shown in Figure 3-17.

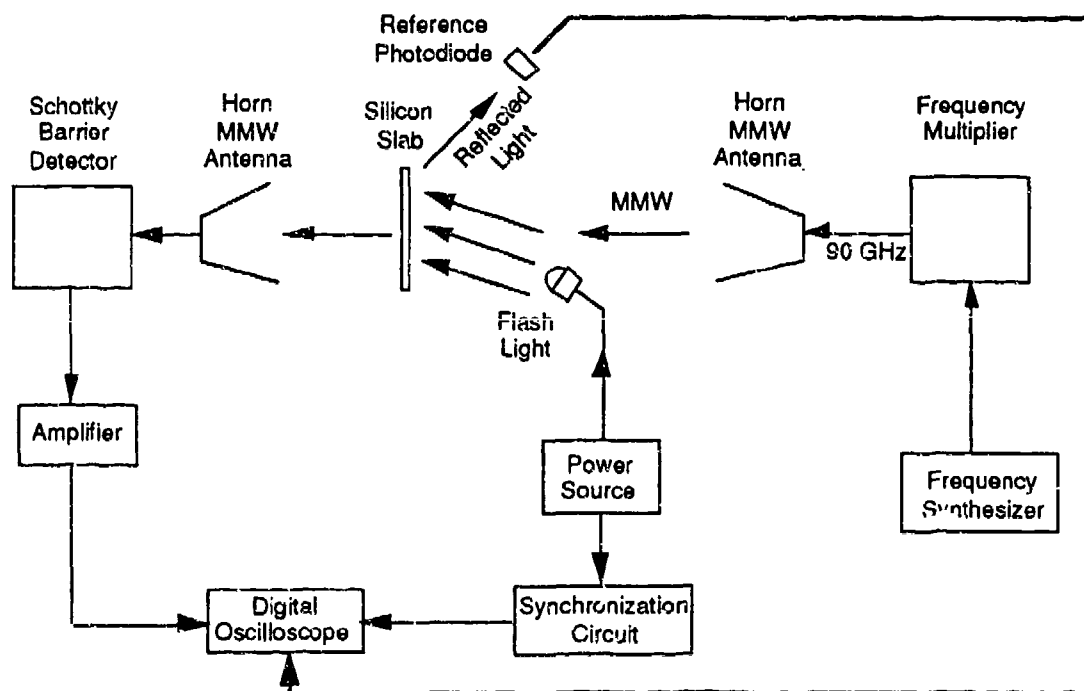


Figure 3-17  
Experimental setup. MMW frequency  $f = 90$  GHz.

We used two silicon slabs with thicknesses of 460  $\mu\text{m}$  and 2 mm, respectively, prepared from a material grown by floating zone technique. The volume carrier lifetime  $\tau_r$  was greater than or equal to  $10^{-3}\text{s}$ .

The setup consisted of a MMW transmitter (which included a frequency synthesizer, a frequency multiplier and a horn antenna), a MMW receiver (which included a horn antenna, a Schottky diode detector and a low frequency amplifier), a pumping light (with a power source and a synchronization circuit), a digital oscilloscope, and a silicon slab with a MMW aperture (not shown in Figure 3-17).

The shape and intensity of the pumping pulse were measured with the reference photodiode. The experimentally obtained oscillograms are shown in Figures 3-18 to 3-20.

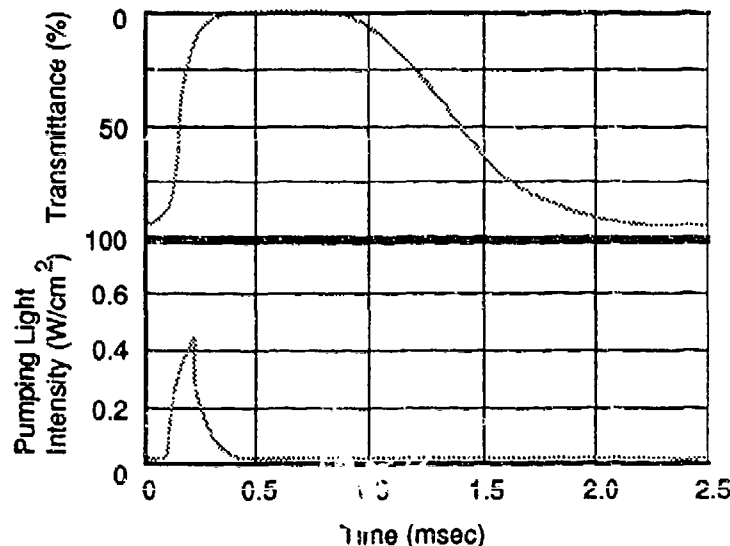


Figure 3-18  
Oscillograms of MMW transmittance (upper trace) and pumping light intensity (lower trace).  
The wafer thickness was  $d = 2 \text{ mm}$ , the pumping pulse duration was  $t_p = 100 \mu\text{sec}$ ,  
and the peak light intensity was  $I_p \approx 400 \text{ mW/cm}^2$ .

According to the data shown in Figure 3-18, a pumping pulse with an energy of  $\sim 4 \times 10^{-5} \text{ J/cm}^2$  caused a deep suppression of the MMW transmittance.

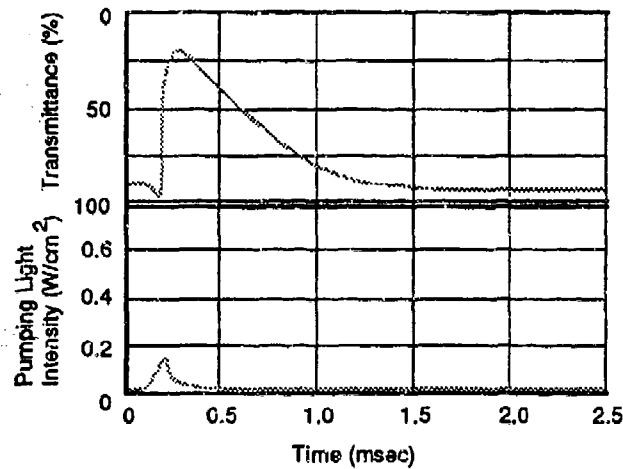


Figure 3-19  
Same as Figure 3-18, but  $I_p = 180 \text{ mW/cm}^2$ .

Figure 3-19 shows that 90% modulation of the MMW transmittance was achieved with pumping pulses of  $\sim 2 \times 10^{-5} \text{ J/cm}^2$ .

According to the theory we developed, the surface recombination causes the illumination to be weaker in thin wafers. The experimental results are in full agreement with the theory. Figure 3-20 shows the data obtained for a 460  $\mu\text{m}$  thick silicon wafer.

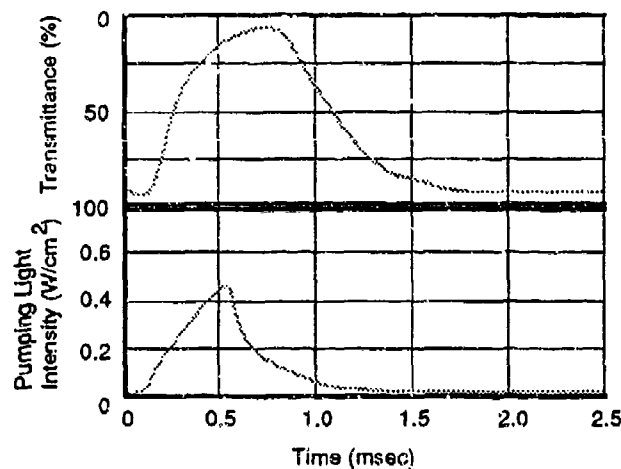


Figure 3-20  
Same as Figure 3-18, but  $d = 0.46 \text{ mm}$ .



According to this data, 95% modulation can be achieved with a pumping pulse of  $5 \times 10^{-4}$  J/cm<sup>2</sup>, which is 2.5 times more than required for the same modulation in a 2 mm thick wafer.

In summary, our experimental data is in good agreement with the developed theory. Thus, we feel confident in continuing our development of MMW antennas based on the concept on which this project was begun.

### **3.3 Summary of Phase I Results**

Phase I research proves that it is possible to modulate MMW radiation through light induced changes in semiconductor material. Specifically, in Phase I POC

- Developed a theoretical model that predicts changes in the MMW dielectric permittivity resulting from the illumination of a semiconductor by light.
- Calculated the required semiconductor parameters (resistivity, carrier life time, surface and volume recombination rates), as well as wavelength and pulse duration of the illuminating light, that will maximize MMW modulation.
- Experimentally demonstrated that MMW transmittance (reflectance) can be dramatically changed if the silicon mask through which the MMW beam propagates is illuminated by the proper light.
- Established solid theoretical and experimental grounds for further development.

### **4.0 PHASE II TECHNICAL OBJECTIVES**

The overall goals of the Phase II project are to develop a generic MMW scanning antenna technology based on the proposed approach, to demonstrate two prototype MMW antennas -- receiver and transmitter -- controlled by light, and to develop a two-dimensional scanning design. The following objectives have been established to meet these goals in the Phase II project.

The technical objectives for the development of MMW beamscanning technology in Phase II are to

- Extend the theory for the selected antenna design and develop a non-stationary theoretical model for pulsed illumination.
- Design a one-dimensional scanning antenna, including all necessary MMW generating/receiving and guiding elements, the optical illuminating and pattern-generating system, and the coupling and anti-reflection components.
- Extend the developed technology to two-dimensional scanning.

The technical goals for the Phase II device demonstration are to

- Fabricate and test the packaged prototype transmitting and receiving MMW antennas. The purpose of these prototypes is to demonstrate flexible beamscanning based on POC's novel concept. These prototypes will be designed for use in MMW scanning systems.
- Demonstrate GAIL technological advances and its readiness to use MMIC and/or semiconductor integrated technology for antenna fabrication. This goal specifically includes design and fabrication of the integrated V-coupler which integrates the MMW detector into the waveguide structure.

Although the proposed Phase II project will focus on one practical embodiment of POC's GAIL, the objectives are aimed at building a solid foundation for this new technology, so that a set of commercial products can be developed for diverse applications. This broad scope of technological development will advance GAIL's commercial potential, thus enhancing the attraction of follow-on funding.

## 5.0 REFERENCES

1. Steinberg, B. D., and Subbaran, H. M. 1991. Microwave Imaging Techniques. New York: John Wiley & Sons, Inc.
2. ROW Smart Weapons Reference Book, U.S. Army Materiel Command, Redstone Arsenal, AL, 1992.

3. Infrared and Millimeter Waves, Edited by K. J. Button and J. C. Wiltse, V. 4, Academic Press, NY, 1981.
4. L. Sadovnik, V. Manasson, and T. Jansson, "Light Controlled Spatial and Angular Electromagnetic Wave Modulator," U.S. Patent S/N: 818,805, allowed (1993).
5. Sze, S. M., Physics of Semiconductor Devices, 2nd Ed., New York: John Wiley & Sons (1981).
6. Palik, E., Handbook of Optical Constants of Solids, Orlando: Academic Press, Inc. (1985).